

Imaging the evolution of metallic states in a correlated iridate

Yoshinori Okada^{1†}, Daniel Walkup¹, Hsin Lin², Chetan Dhital¹, Tay-Rong Chang³, Sovit Khadka¹, Wenwen Zhou¹, Horng-Tay Jeng^{3,4}, Mandar Paranjape¹, Arun Bansil², Ziqiang Wang¹, Stephen D. Wilson¹ and Vidya Madhavan^{1*}

The Ruddlesden–Popper series of iridates ($\text{Sr}_{n+1}\text{Ir}_n\text{O}_{3n+1}$) have been the subject of much recent attention due to the anticipation of emergent phenomena arising from the cooperative action of spin-orbit-driven band splitting and Coulomb interactions^{1–3}. However, an ongoing debate over the role of correlations in the formation of the charge gap and a lack of understanding of the effects of doping on the low-energy electronic structure have hindered experimental progress in realizing many of the predicted states^{4–9}. Using scanning tunnelling spectroscopy we map out the spatially resolved density of states in $\text{Sr}_3\text{Ir}_2\text{O}_7$ (Ir327). We show that its parent compound, argued to exist only as a weakly correlated band insulator, in fact possesses a substantial ~ 130 meV charge excitation gap driven by an interplay between structure, spin-orbit coupling and correlations. We find that single-atom defects are associated with a strong electronic inhomogeneity, creating an important distinction between the intrinsic and spatially averaged electronic structure. Combined with first-principles calculations, our measurements reveal how defects at specific atomic sites transfer spectral weight from higher energies to the gap energies, providing a possible route to obtaining metallic electronic states from the parent insulating states in the iridates.

Spin-orbit-coupled materials are at the forefront of the ongoing search for fundamentally new electronic states. The helical Dirac states of topological insulators^{10,11} and exotic magnetic states¹² such as skyrmion lattices¹³ are recent direct manifestations of spin-orbit coupling. Most of these materials however are well described by single-particle physics, with correlations playing a negligible role in determining their properties. A new frontier in this search, with many predictions of as yet undiscovered phases, is the exploration of materials where spin-orbit coupling and correlations are both relevant. The $5d$ transition-metal iridium oxides (iridates) have been proposed as excellent candidates for materials in this category^{1–3}.

Correlations in the $5d$ and $4d$ transition-metal oxides are expected to be weaker than in their $3d$ counterparts. Following this expectation, many $3d$ transition-metal oxides show Mott insulating ground states¹⁴, whereas the $4d$ ruthenates show mostly metallic behaviour. Surprisingly, despite the anticipation of even weaker correlation effects in the $5d$ compounds, many iridates exhibit magnetic, non-metallic properties^{1–3}. The concept proposed to explain the origin of the insulating behaviour of $5d$ iridates is that the stronger spin-orbit interaction (SOI) creates additional band splitting, resulting in narrow bands close to the Fermi energy,

thereby enhancing correlation effects^{1–3}. In fact, when correlations are strong enough, a new SOI-driven $J_{\text{eff}} = 1/2$ Mott insulator (spin-orbit Mott insulator) is predicted to emerge^{1–4}. This idea has led to theoretical proposals of exciting emergent phenomena including the potential appearance of high- T_c superconductivity⁷. So far, however, the validity and universality of this concept in the $5d$ iridates has been under intense debate^{15–18}.

Amongst the iridate families, the Ruddlesden–Popper series ($\text{Sr}_{n+1}\text{Ir}_n\text{O}_{3n+1}$) goes through a transition from an insulator to a metal with increasing n . Within this series the $n = 2$ compound $\text{Sr}_3\text{Ir}_2\text{O}_7$ (Ir327) occupies a unique place, straddling a well-defined insulator ($n = 1$) on one side and a metal ($n = \infty$) on the other^{3,16}. This places Ir327 in close proximity to a delicate transition point where the interplay between the comparable energy scales of spin-orbit and on-site Coulomb interactions (U) can produce unusual effects within the charge and spin degrees of freedom. Experimental results on Ir327 (refs 3,18,19) including transport, diffraction, and optical spectroscopy demonstrate multiple correlated order parameters and phase transitions indicative of a ground state paralleling those found in their strongly correlated $3d$ transition-metal counterparts. However, the role of correlations remains controversial, with recent suggestions that the material is a simple band insulator with only weak residual correlations⁹. Furthermore, contradictory experimental reports have made the resolution of these issues even more difficult. For example, optical spectroscopy measurements reveal a negligible gap in Ir327 (ref. 3), whereas recent angle resolved photoemission spectroscopy data show indications of a substantially larger gap^{20,21}. The inherent complexities arising from the fact that Ir327 is potentially close to a Mott transition including the tendency for electronic inhomogeneity often seen in such systems^{22,23} have created experimental challenges resulting in important unanswered questions on the actual gap size, the role of correlations, and the influence of defects and dopants on the low-energy density of states (DOS).

Spatially resolved DOS measurements across the Fermi energy, which can provide key information for resolving these issues have not yet been performed on the iridates. In this work, we measure single crystals of Ir327 with scanning tunnelling microscopy (STM) and spectroscopy. Our local DOS maps ($\text{LDOS}(r, eV) = dI/dV(r, eV)$) reveal an inhomogeneous, textured electronic landscape. Within the spatially varying DOS, we identify the intrinsic DOS of Ir327 with a hard gap of ~ 130 meV. Comparisons with generalized gradient approximation (GGA) + U

¹Department of Physics, Boston College, Chestnut Hill, Massachusetts 02467, USA, ²Physics Department, Northeastern University, Boston, Massachusetts 02115, USA, ³Department of Physics, National Tsing Hua University, Hsinchu 30013, Taiwan, ⁴Institute of Physics, Academia Sinica, Taipei 11529, Taiwan. [†]Present address: WPI-AIMR, Tohoku University, Sendai, 980-8577, Japan. *e-mail: madhavan@bc.edu

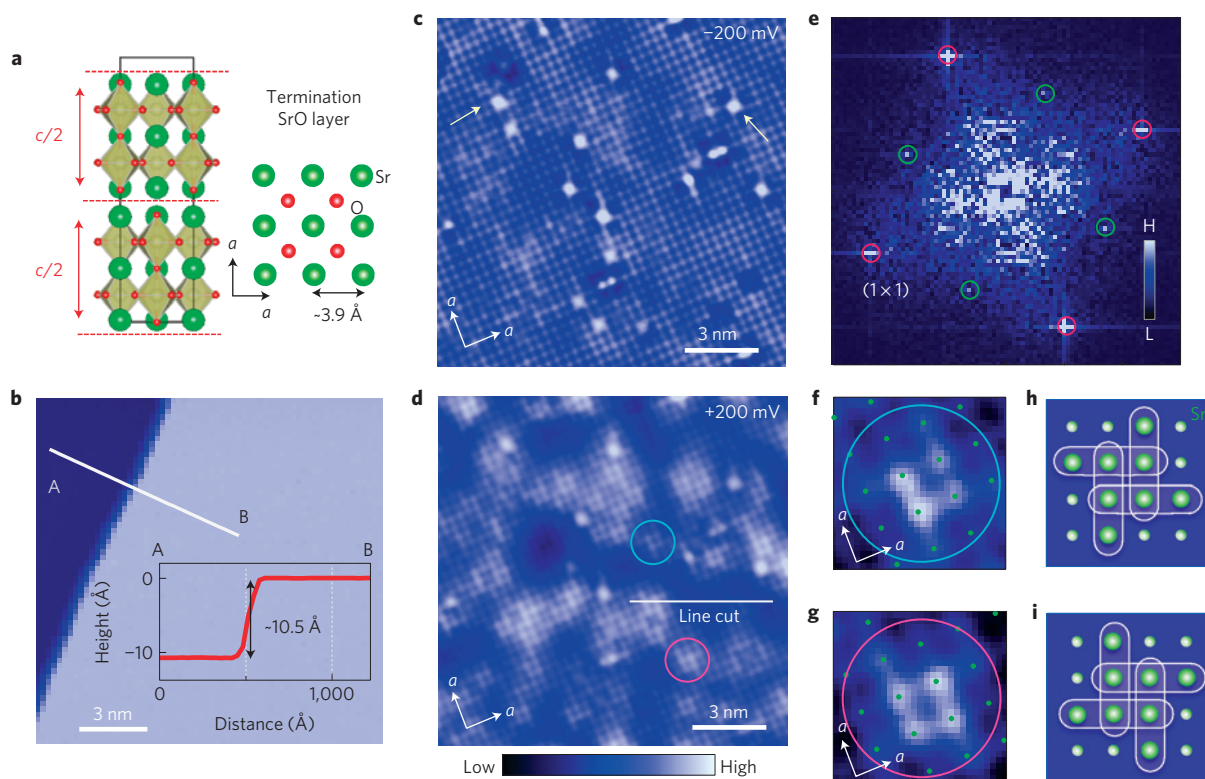


Figure 1 | Topographic images of $\text{Sr}_3\text{Ir}_2\text{O}_7$. **a**, Crystal structure of $\text{Sr}_3\text{Ir}_2\text{O}_7$. **b**, Typical step edge in topography, whose step height is half of the unit cell as indicated by the arrows in **a**. **c**, Topographic image at bias voltage $V_B = -200$ mV. **d**, Topography at $V_B = +200$ mV in the same area as in **c**. The two typical types of chemical disorder are indicated by circles and arrows in **c, d**. **e**, Fourier transform of **c**, showing Bragg peaks representing 1×1 (pink circles) and $\sqrt{2} \times \sqrt{2}$ (blue circles) order. **f, g**, Square-shaped defects with two different chiralities. Topographic lattice sites are indicated by dots. **h, i**, Schematic representation of chiral defects shown in **f, g**. The green circles represent the atoms seen in the termination SrO layer.

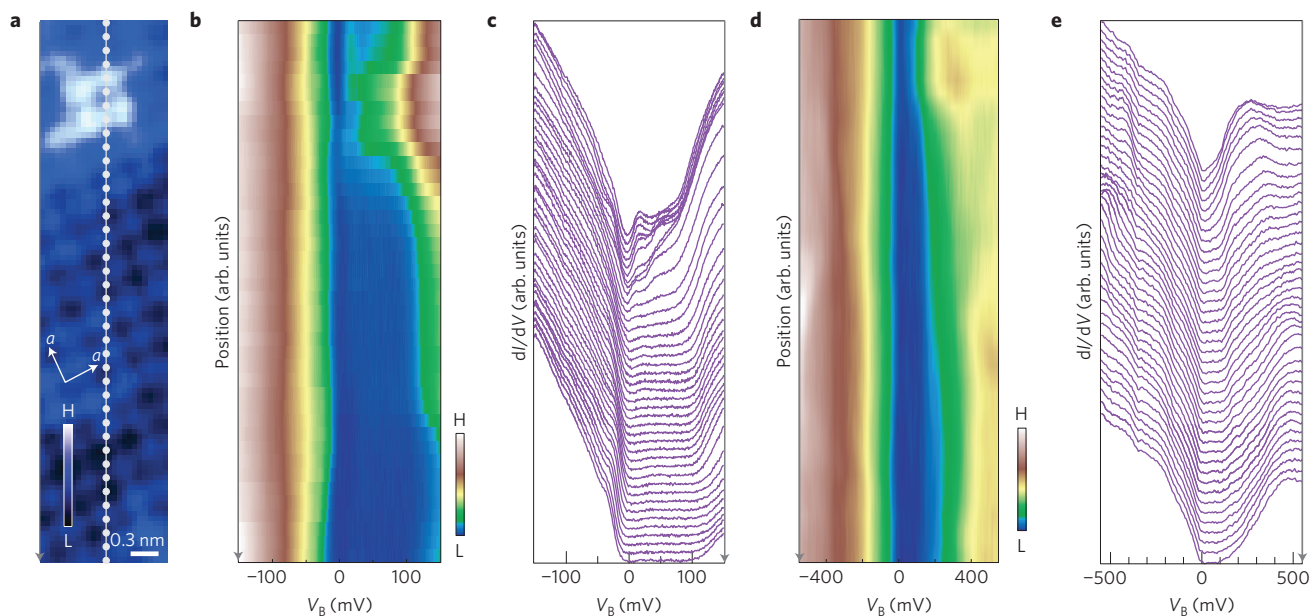


Figure 2 | Tunneling spectra across a chemical defect. **a**, A section of the topographic image shown in Fig. 1d (bias voltage $V_B = +200$ mV) where the line cuts shown in **c, e** were obtained. **b**, Intensity plot of the conductance values in the line cut shown in **c, e**. **c**, Tunneling spectra along the line shown in **a** over a narrow energy range with energy resolution ~ 1 meV. **d**, Intensity plot of the conductance values in the line cut shown in **e**. **e**, Tunneling spectra along the line shown in **a**, over a wide energy range with ~ 10 meV resolution.

calculations clearly show that this gap arises from a combination of rotated oxygen octahedra, enhanced spin-orbit coupling and Coulomb interactions, with each playing a critical role in

determining the low-energy DOS. The data further reveal that the metallic regions are correlated with single-atom defects offering a unique opportunity to determine how defects at particular lattice

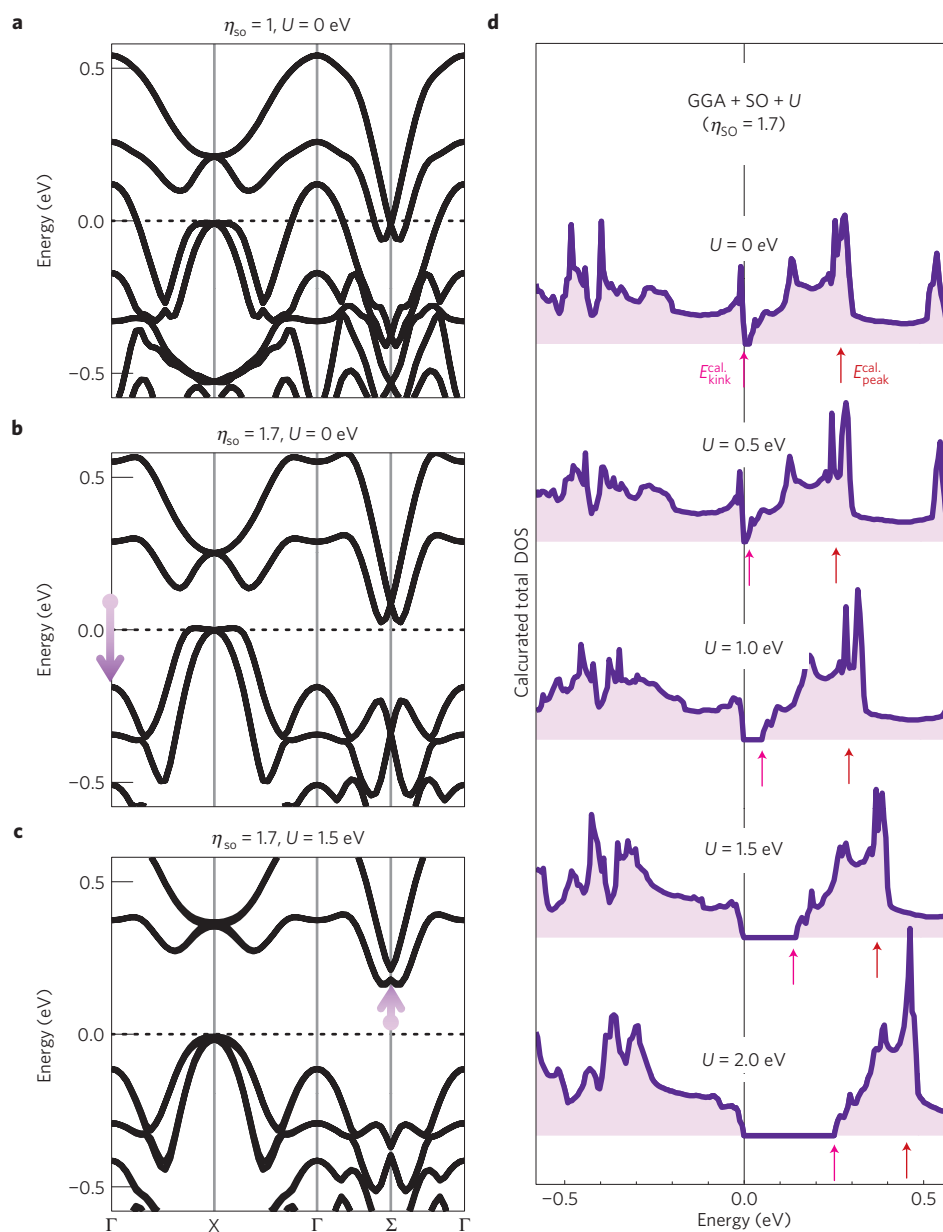


Figure 3 | GGA + U band calculation along high-symmetry lines. **a**, Band structure with spin-orbit coupling obtained self-consistently. **b**, Band structure with enhanced spin-orbit (SO) coupling. Here, $\eta_{\text{SO}} = 1.7$ represents a spin-orbit strength that is 1.7 times the GGA + U self-consistently obtained value. **c**, Band structure with on-site energy $U = 1.5$ (eV) added to **b**. **d**, LDOS calculations for different values of Coulomb U . The pink and red arrows refer to $E_{\text{kink}}^{\text{calc}}$ and $E_{\text{peak}}^{\text{calc}}$, respectively.

sites alter the local DOS from insulating to metallic. These data provide critical information for tuning the low-energy electronic structure of iridates; an important component for realizing emergent phases such as superconductivity. Equally importantly, this STM study of the iridates opens the doors to STM investigations of this important family of compounds.

Single crystals of $\text{Sr}_3\text{Ir}_2\text{O}_7$ were grown using flux techniques similar to earlier reports¹⁹. The Ir327 single crystals thus prepared were cleaved at ~ 77 K in ultrahigh vacuum before being directly transferred to the STM head held at 4 K. Figure 1 shows STM topographic images of the surface. Similar surfaces were reproducibly imaged on multiple samples by different tips as long as the crystals were cleaved at low temperatures. The natural cleaving plane is in between the perovskite bilayer structure, whose unit length along the c axis corresponds to half of the lattice constant c (Fig. 1a,b). Cleaving is expected to result in the exposure of the strontium oxide

(SrO) plane (Fig. 1a). The topography (Fig. 1c,d) and its Fourier transforms (Fig. 1e) show a 1×1 square lattice of atoms separated by 3.9 Å, which is equal to the separation between either strontium or apical oxygen atoms. The Fourier transform of the topography also shows peaks at the $\sqrt{2} \times \sqrt{2}$ positions (Fig. 1e). Similar features in the isostructural ruthenate $\text{Sr}_3\text{Ru}_2\text{O}_7$ were attributed to two possible causes, either the broken symmetry arising from alternating rotations of the oxygen octahedra surrounding the Ru atoms²⁴, which also exists for Ir327 samples, or a charge-density wave (CDW) formation on the surface²⁵. In our case, as the $\sqrt{2} \times \sqrt{2}$ structure persists to high energies, it cannot be attributed to a simple CDW. Although the actual origin of the $\sqrt{2} \times \sqrt{2}$ structure is not completely clear, as this topographic feature has no bearing on the main points of the present study, we do not pursue it any further in this paper. The topographic images show two types of chemical disorder; the bright dots and the square-shaped patterns

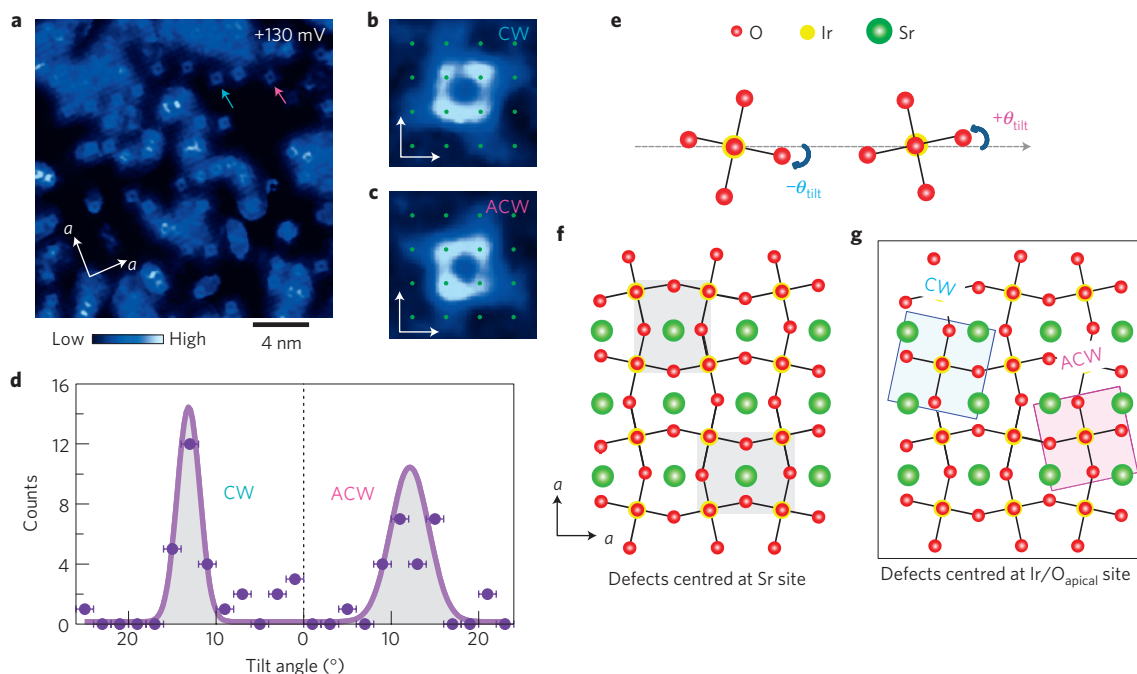


Figure 4 | Visualization of the rotation angles of the underlying iridium oxide layer through crystal defects. **a**, dI/dV map at +130 mV showing the LDOS signatures of the chiral defects shown in Fig. 1. Note that this area is different from Fig. 1c,d. **b,c**, dI/dV maps of two defects rotated clockwise (CW) and anticlockwise (ACW) from the in-plane Sr–O bond direction. The dots are the locations of the atoms from the simultaneously recorded topography. **d**, Histogram of the rotation (in-plane tilt) angles obtained from impurities in **a** (see main text and Supplementary Information for more details). The error bars, estimated to be ± 1 degrees, arise from the standard deviation of the tilt angle for each defect obtained during the fitting procedure described in the Supplementary Discussion (Fig. S2d). **e**, Schematic drawing representing the characteristic tilt angle $\pm\theta_{\text{tilt}}$, which is the in-plane O–Ir–O bond angle. **f,g**, Schematic top view of the SrO layer and the IrO layer. The expected local symmetry of the two inequivalent sites centred on Sr (**f**) and centred on the Ir or apical oxygen site (**g**).

indicated by arrows in Fig. 1c and circles in Fig. 1d, respectively. The bright dots are most likely adsorbed impurities on top of the surface and can be attributed to either excess Sr or oxygen atoms probably resulting from the cleaving process. On the other hand, the defects shown in Fig. 1f–i (square-shaped defects with two different chiralities) arise from embedded surface or sub-surface defects whose identity will be discussed in greater detail later in this paper.

Whereas the topographies at negative voltages (Fig. 1c) are reasonably homogeneous, those at positive voltages (Fig. 1d) show bright and dark patches indicating a highly inhomogeneous electronic structure with a characteristic length scale of a few nanometres. To understand the origins of this inhomogeneity and the behaviour of the DOS, we plot the tunnelling spectra obtained along a line cut across a chiral defect as shown in Fig. 2a. We find that the LDOS exhibit pronounced changes across defects, evolving from spectra showing almost zero LDOS near E_F (spectra close to bottom in Fig. 2c,e) to more a metallic V-shape (spectra close to the top in Fig. 2). This poses the question: what is the intrinsic DOS of the parent compound of Ir327 and what is responsible for this inhomogeneity? In semiconductors and insulators with poor screening, random dopant distribution is often responsible for electronic inhomogeneity. In our case, although the material is not deliberately doped, there are naturally occurring defects that may potentially be responsible for this behaviour. Comparing the STM topography (Fig. 2a) to the spectral line cut (Fig. 2b–e), it is clear that the V-shaped LDOS is correlated with the presence of the square-shaped chiral defect. In contrast, the spectra away from defects exhibit a highly suppressed (approximately zero) LDOS from ~ 10 meV below the E_F to ~ 120 meV above E_F (Fig. 2b,c). Zooming out to a wider energy range (Fig. 2d,e) we find that these regions show a semiconducting/insulating line shape with the E_F positioned very close to a band edge. This indicates that the intrinsic

DOS in the ground state of the parent Ir327 system is a ~ 130 meV hard-gap insulator.

Having determined the intrinsic DOS of parent Ir327, we address the role and importance of correlations in determining the electronic structure of this system. GGA + U calculations of the band structure (Fig. 3a–c) and the DOS for various values of U (Fig. 3d) are shown in Fig. 3. As per our calculations, increasing both spin–orbit (which lowers the occupied band at Γ as shown in Fig. 3b) and on-site U (which raises the unoccupied band at the Σ point, as shown in Fig. 3c) are needed to explain the experimentally observed gap in the LDOS near the Fermi energy (also see Supplementary Discussion for more details). We note here that the calculations were performed within a larger parameter space by varying the spin–orbit coupling as well as the octahedral in-plane tilt angle (within realistic deviations of a few degrees from the measured values), and the best fit parameters (value of U between 1.5 and 2.0 eV) were determined to match the recent angle-resolved photoemission spectroscopy reports of band dispersion^{20,21} as well as the STM gap. Although GGA + U calculations are not expected to capture the quantitative magnitude of the gap, the failure of the $U = 0$ calculation to open a substantial charge excitation gap indicates that the crystal-field effects combined with strong spin–orbit coupling are grossly insufficient to create a gap of the magnitude observed by us. Thus, the conclusion of our studies is that correlations are critical to understanding the band structure of the parent iridate Ir327. The natural question then is how does this correlated band structure evolve into the more metallic DOS?

To answer this question we focus on the V-shaped LDOS related to the chiral defects. Our first task is to determine their chemical identity. As shown in Fig. 1f–i, these defects retain C_4 symmetry while breaking reflection symmetry locally, and are aligned along the high-symmetry directions of the lattice seen in the STM

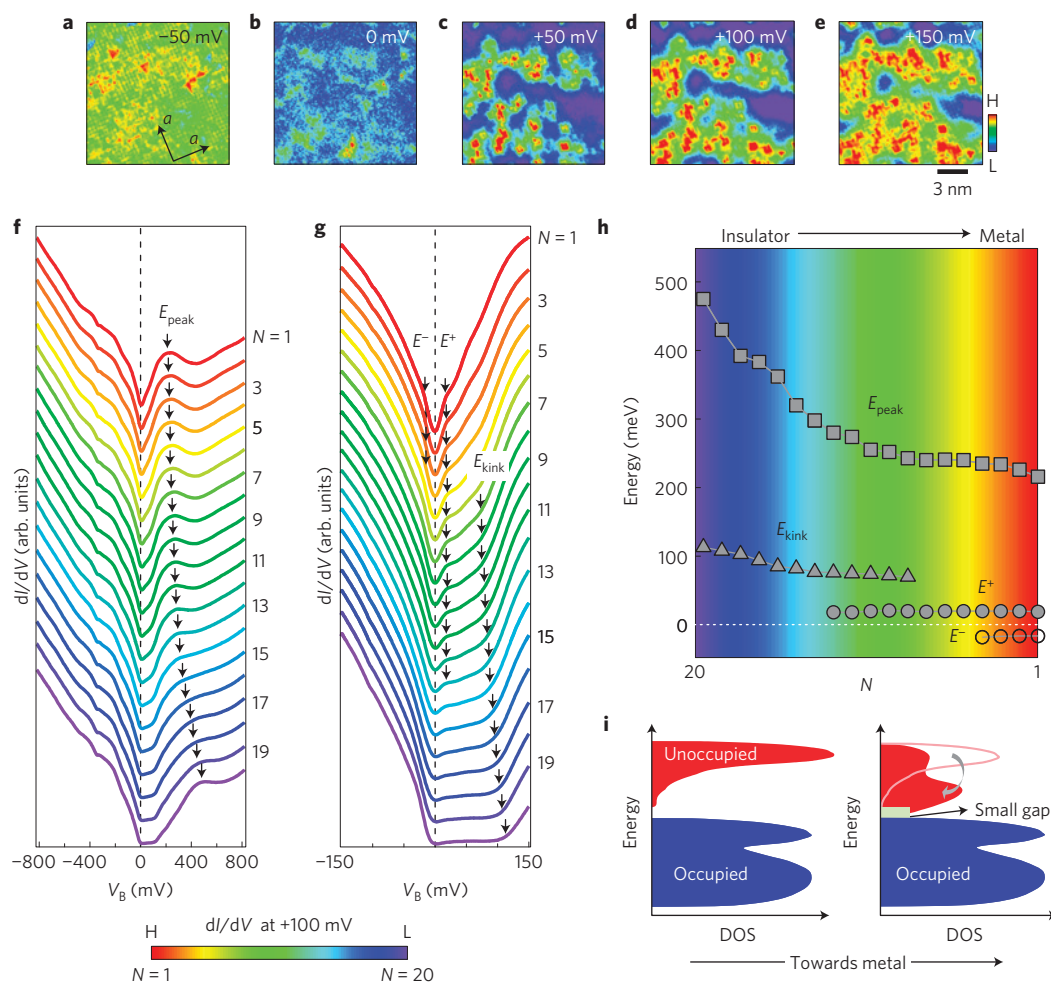


Figure 5 | Spatial evolution of tunnelling spectra. **a–e**, Energy dependence of conductance map obtained in the same area shown in Fig. 1c,d. **f,g**, Averaged spectra classified by values of conductance at +100 mV. Here, spectra are split into 20 groups with equal population, from highest ($N=1$, red) to lowest ($N=20$, blue) conductance. **f**, Narrow energy spectra with higher energy resolution (~ 1 meV). **g**, Wide energy spectra (with ~ 10 meV resolution). **h**, Evolution of the characteristic energy scales (E_{peak} , E^+ , E^- and E_{kink}) represented by arrows in **f,g** shown as a function of N . **i**, Schematic spectral evolution based on experimental data.

topographic images (green dots in Fig. 1f–i). One might imagine that the different chiralities (Fig. 1f,g) indirectly reflect the in-plane octahedral rotations that lead to two inequivalent lattice sites²⁴. In our case, the validity of this conjecture can be directly visualized by analysing the LDOS maps. As shown in Fig. 4a, positive-energy LDOS maps reveal square-shaped patterns associated with the chiral impurities. Closer examination shows that unlike their shapes in the topography, the LDOS squares are not aligned with the lattice and are in fact distinctly rotated about the c axis in either a clockwise or anticlockwise manner with respect to the a axis as shown in Fig. 4b,c. Plotting the histogram of rotation angles as measured from the a axis (Fig. 4d), we find a bimodal distribution of $(12.5 \pm 2)^\circ$. The bimodal nature of the rotations and the closeness of this absolute value to the measured in-plane octahedral rotation angle ($\sim 12^\circ$) from X-ray diffraction²⁶ indicate that our LDOS maps capture the local symmetry of the iridium oxide planes (Fig. 4e–g). Interestingly, octahedral-rotation-related signatures have also been beautifully visualized locally using STM in the isostructural system Ti-doped $\text{Sr}_3\text{Ru}_2\text{O}_7$ (ref. 24). A comparison between the defects in the two compounds, which may be of interest to theorists modelling microscopic disorder in correlated materials, is presented in Supplementary Sections S2 and S3.

On the basis of the experimentally observed rotational symmetry of the defects, we rule out the possibility that these impurities are

centred at Sr sites (Fig. 4f), which do not reflect the $\sim 12^\circ$ octahedral rotation. Instead, we identify the defect centre position with either the apical oxygen site in the SrO plane or the Ir site in the IrO_2 plane (Fig. 4g). Although Ir site defects cannot be completely ruled out, oxygen vacancies are common defects in layered oxides and are also potentially created during the cleaving process, making it more likely that these defects represent vacancies at the apical oxygen sites. This is consistent both with transport data showing increasing metallicity with increasing apical oxygen vacancy concentration in iridates²⁷ and with our calculations on the effects of apical oxygen vacancies on the DOS discussed next. We note here that one of the most difficult tasks in an STM experiment is to identify the chemical identity of the imaged atoms. However, as shown here, using LDOS patterns reflecting the symmetry of the underlying lattice provides an as yet unexplored method of determining the identity of imaged atoms. In this case, for example, the identification of the impurity centre site within the lattice enables us to determine that the imaged atoms in the topography must be Sr atoms, laying to rest the controversy of which atom is imaged in STM topographies of SrO surfaces in the ruthenates and iridates.

We are now ready to discuss the effects of the chiral defects on the low-energy DOS. In many oxides, including the cuprates, atomic-scale defects, and in particular apical oxygen vacancies, play a critical role in determining the functionality of the system^{27–30}.

Our ability to locate and measure the DOS at potential apical oxygen sites provides us with a unique opportunity to determine their effects as a function of both position and energy. To do this systematically, we analyse the LDOS in the region shown in Fig. 1c,d. First, by comparing the topographic images (Fig. 1c,d) and the LDOS maps (Fig. 5a–e), as well as by performing a cross-correlation analysis (Supplementary Fig. S3), we see that the higher DOS regions (red) are indeed statistically correlated with the vacancy locations. The spatial distribution of the DOS thus suggests a method to obtain a systematic picture of the effects of these vacancies on the DOS by categorizing the corresponding spectra on the basis of conductance values. We first classify all of the spectra obtained in this region into 20 groups based on the conductance at +100 mV (also see Supplementary Fig. S5 for more details) and then average the spectra within each category. The averaged spectra are shown in Fig. 5f,g. Here, $N = 1$ represents the index for the highest and therefore most metallic LDOS (top red spectra in Fig. 5f,g) and $N = 20$ represents the index for close to zero, that is, insulating LDOS (bottom purple spectra in Fig. 5f,g). By comparing the topographic images (Fig. 1c,d), LDOS maps (Fig. 5a–e) and the LDOS spectral shapes (Fig. 5f,g), we confirm that areas with the ~ 130 meV hard gap ($N = 20$, coloured purple) are always observed away from defects whereas the V-shaped, metallic LDOS ($N = 1$, also the red regions) are centred around the defect sites. On further examination of the spectra, we identify four characteristic energy scales (E_{peak} , E_{kink} , E^+ and E^-) indicated by arrows in Fig. 5f,g. Plotting these as a function of N reveals how these energy scales evolve with the crossover from an insulator to a metal (Fig. 5h). Focusing on the spectral evolution of V-shaped metallic LDOS ($N = 1$) from underlying parent LDOS ($N = 20$), we find that the spectral weight transfer occurs continuously over a wide energy region, as schematically shown in Fig. 5i. From these data it is clear that the LDOS evolution (Fig. 5f–h) cannot be understood in terms of a simple filling change within a rigid band picture.

A qualitative insight into the trends in E_{peak} and E_{kink} can be obtained by our GGA + U and slab calculations. As shown in the GGA + U calculations in Fig. 3c (also Supplementary Discussion), both the gap size (labelled $E_{\text{kink}}^{\text{calc}}$) and the peak energy (labelled $E_{\text{peak}}^{\text{calc}}$) shift towards E_F with decreasing U , mimicking the experimentally observed LDOS evolution (Fig. 5f–h). However, we note that as U is treated at a mean field level in GGA + U , the main effect of correlations in GGA + U is to renormalize the crystal-field splitting in an orbital-dependent manner. Thus, in addition to charge doping, the defect-induced changes in the crystal fields may be indirectly reflected by the U in the GGA + U calculations (see Supplementary Discussion for a detailed discussion). Preliminary slab calculations indicate that in the absence of the apical oxygen, the Ir atoms shift towards the missing oxygen site and metallic bands are formed at the Ir atom below the vacancy owing to a downshift of the conduction bands (Supplementary Fig. S9). The calculations are consistent with the identification of the chiral defects with apical oxygen vacancies and indicate that the low-energy DOS in Ir327 is highly sensitive to small changes in local parameters brought about by the distortion created by vacancies. The sensitivity of the band structure indicates the tunable nature of the 327 compounds, an important aspect in realizing emergent phases at the boundary of a destabilized SOI-driven correlated insulator.

On a final note, we comment on the energy scales E^+ and E^- that emerge as the system gets more metallic, and get progressively more symmetric about the Fermi energy. These features are not seen in the GGA calculations. Although the origin of this intriguing particle–hole symmetric gap-like feature is far from clear, this complex behaviour with multiple emergent energy scales is unlike the disorder-induced bound-states picture in a simple band insulator. These trends are instead reminiscent

of observations in correlated 3d transition-metal oxides^{14,31–33} where the LDOS evolves quite markedly from the parent Mott insulating state owing to the complex many-body effects associated with strong correlations.

Received 15 November 2012; accepted 12 April 2013;
published online 26 May 2013

References

- Kim, B. J. *et al.* Novel $J_{\text{eff}} = 1/2$ Mott state induced by relativistic spin–orbit coupling in Sr_2IrO_4 . *Phys. Rev. Lett.* **101**, 076402–076405 (2008).
- Kim, B. J. *et al.* Phase-sensitive observation of a spin–orbital Mott state in Sr_2IrO_4 . *Science* **323**, 1329–1332 (2009).
- Moon, S. J. *et al.* Dimensionality-controlled insulator–metal transition and correlated metallic state in 5d transition metal oxides $\text{Sr}_{n+1}\text{Ir}_n\text{O}_{3n+1}$ ($n = 1, 2$, and ∞). *Phys. Rev. Lett.* **101**, 226402–226405 (2008).
- Jackeli, G. & Khaliullin, G. Mott insulators in the strong spin–orbit coupling limit: From Heisenberg to a quantum compass and Kitaev models. *Phys. Rev. Lett.* **102**, 017205–017208 (2009).
- Shitade, A. *et al.* Quantum spin Hall effect in a transition metal oxide Na_2IrO_3 . *Phys. Rev. Lett.* **102**, 256403–256406 (2009).
- Wan, X. *et al.* Topological semimetal and Fermi-arc surface states in the electronic structure of pyrochlore iridates. *Phys. Rev. B* **83**, 205101–205109 (2011).
- Wang, F. & Senthil, T. Twisted Hubbard model for Sr_2IrO_4 : Magnetism and possible high temperature superconductivity. *Phys. Rev. Lett.* **106**, 136402–136405 (2011).
- Pesin, D. & Balents, L. Mott physics and band topology in materials with strong spin–orbit interaction. *Nature Phys.* **6**, 376–381 (2010).
- Carter, J. M., Shankar, V. V. & Kee, H. Y. Theory of magnetic structure in layered iridates: Spin–orbit band or Mott insulators. Preprint at <http://arxiv.org/abs/1207.2183> (2012).
- Kane, C. L. & Mele, E. J. Z_2 topological order and the quantum spin Hall effect. *Phys. Rev. Lett.* **95**, 146802–146805 (2005).
- Hasan, M. Z. & Kane, C. L. Topological insulators. *Rev. Mod. Phys.* **82**, 3045–3067 (2010).
- Nagaosa, N. & Tokura, Y. Emergent electromagnetism in solids. *Phys. Scr.* **T146**, 014020–014035 (2012).
- Mühlbauer, S. *et al.* Skyrmion lattice in a chiral magnet. *Science* **323**, 915–919 (2009).
- Imada, M., Tokura, Y. & Fujimori, A. Metal–insulator transition. *Rev. Mod. Phys.* **70**, 1039–1263 (1998).
- Hsieh, D. *et al.* Observation of a metal-to-insulator transition with both Mott–Hubbard and Slater characteristics in Sr_2IrO_4 from time-resolved photocarrier dynamics. *Phys. Rev. B* **86**, 035128 (2012).
- Fujiyama, S. *et al.* Weak antiferromagnetism of $J_{\text{eff}} = 1/2$ band in bilayer iridate $\text{Sr}_3\text{Ir}_2\text{O}_7$. *Phys. Rev. B* **86**, 174414 (2012).
- Arita, R. *et al.* *Ab initio* studies on the interplay between spin–orbit interaction and coulomb correlation in Sr_2IrO_4 and Ba_2IrO_4 . *Phys. Rev. Lett.* **108**, 086403–086406 (2012).
- Cao, G. *et al.* Anomalous magnetic and transport behavior in the magnetic insulator $\text{Sr}_3\text{Ir}_2\text{O}_7$. *Phys. Rev. B* **66**, 214412–214418 (2002).
- Dhital, C. *et al.* Spin ordering and electronic texture in the bilayer iridate $\text{Sr}_3\text{Ir}_2\text{O}_7$. *Phys. Rev. B* **86**, 100401–100404 (2012).
- Wang, Q. *et al.* Dimensionality controlled Mott transition and correlation effects in single- and bi-layer perovskite iridates. Preprint at <http://arxiv.org/abs/1210.4141> (2012).
- Wojek, B. M. *et al.* The $J_{\text{eff}} = 1/2$ Mott insulator $\text{Sr}_3\text{Ir}_2\text{O}_7$ studied by angle-resolved photoemission spectroscopy. *J. Phys.: Condens. Matter* **24**, 415602 (2012).
- Dagotto, E. Complexity in strongly correlated electronic systems. *Science* **309**, 257–262 (2005).
- Pan, S. H. *et al.* Microscopic electronic inhomogeneity in the high- T_c superconductor $\text{Bi}_2\text{Sr}_2\text{CaCu}_2\text{O}_{8+x}$. *Nature* **413**, 282–285 (2001).
- Lee, J. *et al.* Heavy d-electron quasiparticle interference and real-space electronic structure of $\text{Sr}_3\text{Ru}_2\text{O}_7$. *Nature Phys.* **5**, 800–804 (2009).
- Iwaya, K. *et al.* Local tunneling spectroscopy across a metamagnetic critical point in the bi-layer ruthenate $\text{Sr}_3\text{Ru}_2\text{O}_7$. *Phys. Rev. Lett.* **99**, 057208–057211 (2007).
- Subramanian, M. A., Crawford, M. K. & Harlow, R. L. Single crystal structure determination of double layered strontium iridium oxide $\text{Sr}_3\text{Ir}_2\text{O}_7$. *Mater. Res. Bull.* **29**, 645–650 (1994).
- Korneta, O. B. *et al.* Electron-doped $\text{Sr}_2\text{IrO}_{4-\delta}$ ($0 \leq \delta \leq 0.04$): Evolution of a disordered $J_{\text{eff}} = 1/2$ Mott insulator into an exotic metallic state. *Phys. Rev. B* **82**, 115117 (2010).
- Tokura, Y., Takagi, H. & Uchida, S. A superconducting copper oxide compound with electrons as the charge carriers. *Nature* **337**, 345–347 (1989).

29. Ohta, Y., Tohyama, T. & Maekawa, S. Apex oxygen and critical temperature in copper oxide superconductors: Universal correlation with the stability of local singlets. *Phys. Rev. B* **43**, 2968–2982 (1991).
30. Pavarini, E. *et al.* Band-structure trend in hole-doped cuprates and correlation with T_{cmax} . *Phys. Rev. Lett.* **87**, 047003–047006 (2001).
31. Kohsaka, Y. *et al.* Visualization of the emergence of the pseudogap state and the evolution to superconductivity in a lightly hole-doped Mott insulator. *Nature Phys.* **8**, 534–538 (2012).
32. Ye, C. *et al.* Visualizing the atomic scale electronic structure of the $\text{Ca}_2\text{CuO}_2\text{Cl}_2$ Mott insulator. *Nature Commun.* **4**, 1365 (2013).
33. Zhou, S. *et al.* Electron correlation and Fermi surface topology of Na_xCoO_2 . *Phys. Rev. Lett.* **94**, 206401–206404 (2005).

Acknowledgements

V.M. gratefully acknowledges funding from US NSF-CAREER-0645299 for support of D.W., Y.O. and W.Z. S.D.W. acknowledges NSF DMR-1056625 for support of C.D. and S.K. Z.W. acknowledges the DOE grants: DE-FG02-99ER45747 and DOE DE-SC0002554. T.R.C. and H.T.J. are supported by the National Science Council, Taiwan. H.T.J. also thanks NCHC, CINC-NTU and NCTS, Taiwan for technical support.

The work at Northeastern University is supported by the US Department of Energy, Office of Science, Basic Energy Sciences contract DE-FG02-07ER46352, and benefited from Northeastern University's Advanced Scientific Computation Center (ASCC), theory support at the Advanced Light Source, Berkeley and the allocation of supercomputer time at NERSC through DOE grant number DE-AC02-05CH11231.

Author contributions

Y.O. and V.M. designed the experiments. Y.O., M.P., W.Z. and D.W. participated in the experiments. V.M., Y.O., S.D.W., Z.W. and D.W. wrote the paper. C.D. and S.K. made single-crystal samples. Z.W., H-T.J., T-R.C., H.L. and A.B. carried out the theoretical calculations.

Additional information

Supplementary information is available in the [online version of the paper](#). Reprints and permissions information is available online at www.nature.com/reprints. Correspondence and requests for materials should be addressed to V.M.

Competing financial interests

The authors declare no competing financial interests.